

Bi-static Radar Interferometric Localization of MEO and GEO Space Debris using the Australia Telescope Compact Array

Hamed Nosrati

CSIRO Space and Astronomy, Australia

Stephanie Smith¹, Douglas B. Hayman¹, Shinji Horiuchi¹, Andrew Hellicar², and Ken Smart¹

¹ *CSIRO Space and Astronomy, Australia*, ² *CSIRO Data61, Australia*

ABSTRACT

We demonstrate utilizing the Australia Telescope Compact Array (ATCA) for bi-static observation of resident space objects (RSOs) around medium earth orbit (MEO) and geostationary orbit (GEO). We propose a general system model for near-field space observation using a correlator radio telescope featuring post-observation delay-tracking correction and 3D re-focusing. Employing the proposed method, we localize RSOs by forming a 3D range-direction spectrum around the a priori coordinate or cue and estimate a refined range and direction of arrival (DOA). To demonstrate the performance of the proposed model, we designed a bi-static experiment comprising NASA's Canberra Deep Space Communications Complex (CDSCC) transmitter and ATCA. We investigate the measurement system's performance by analyzing the stability of the phase of the visibilities and show the phase precision, which is an indicator of the accuracy of the interferometer's expected coordinate, improves significantly after using the estimated datapoints.

1. INTRODUCTION

Space debris comprises artificial objects left in the Earth's orbit across more than six decades of space activities. The increasing growth of the orbital debris population exhibits a critical risk for existing and upcoming space missions. As a result, there has been an ever-growing interest in expanding the network of available sensors to detect, localize and characterize the space debris in orbit about the Earth to increase and maintain Space Situational Awareness (SSA) [1,2]. Currently, optical, laser ranging and radar sensors constitute the backbone of SSA networks. Complementary to the existing sensors, radio astronomy interferometers featuring extremely high sensitivity, narrow beamwidth, and wide bandwidth offer an excellent opportunity for SSA activities [3, 4].

Considering radio observations for orbit determination, a dedicated mono-static or bi-static radar can potentially provide the range, velocity (Doppler), and direction information. Examples with published specifications include the German Experimental Surveillance and Tracking (GESTRA), the Korea Space Surveillance Active Phased Array Radar Window (KOSPAW), and the LeoLabs radar network [5–7]. In comparison, a radio interferometer can typically provide superior direction but inferior range estimates. An example of such a dedicated radio interferometer is the now retired US Navy Space Surveillance System (NAVSPASUR), colloquially known as space fence, which employed radio interferometry using three transmitters and six receivers [8]. While SSA-dedicated radio interferometers have not been commonly used to provide SSA data products, repurposing existing assets such as radio telescopes allows access to additional SSA data. Radio telescopes have already been employed to provide SSA data products in single-dish radar mode [9–11], or multi-element passive bi-static radar mode, mainly using processed raw voltages from each antenna [12, 13].

In this work, we study the performance of a correlator radio telescope array for providing SSA data products. We develop a system model for interferometry-based localization and present the results based on a series of experiments for resident space object (RSO) location refinement in a bi-static interferometry configuration using NASA's Deep Space Network (DSN) facility located at Tidbinbilla in the Australian Capital Territory (ACT) Australia, and Australia Telescope Compact Array (ATCA) at the Paul Wild Observatory near Narrabri in New South Wales (NSW), Australia.

Two data products of interest from interferometric radio telescopes are 1) raw voltages or baseband signal at each antenna and 2) visibilities or spatial correlation lags at the interferometer's output. To devise a generic method applicable to interferometry systems, we use visibilities as they are the standard data output of most radio astronomy interferometers. We develop a signal and system model for estimating the spatial spectrum, i.e., the direction of arrival (DOA) and range from the visibilities. In particular, we use the interferometry equations and apply offline re-focusing to focus the visibilities, delay-tracked for a solid angle in the far-field, on a grid of ranges near the location of interest. Employing re-focusing, we establish a measurement vector with right ascension (RA), declination (Dec), and range as the unknown variables. We then use the measurement vector in a multiple signal classification (MUSIC) estimator to estimate RA, Dec, and range offsets of the source of interest [14].

We carried out a measurement campaign in June 2021 to demonstrate the capability of the proposed system model. Various pieces of orbital debris around geostationary orbit (GEO) and medium earth orbit (MEO) were illuminated by a 36-meter DSN transmitter, and the reflected signal's spatial correlation was recorded by ATCA. We employ the proposed technique on the recorded data and provide preliminary estimates for direction and range. Using the estimated location datapoints, we investigate the measurement system's performance by analyzing the stability of the phase of the visibilities and show the phase stability improves significantly after using the estimated ephemerides.

2. PROBLEM FORMULATION

This section develops a signal model for estimating range and DOA (RDOA) from the visibilities. For a set of baselines defined in the uvw coordinate system within the terrestrial frame, the interferometer's output at a certain subband for a source located in the far-field region is modeled as [15]

$$v(u, v) = \int_{-\infty}^{\infty} \int_{-\infty}^{\infty} A_f(l, m) I_f(l, m) e^{-j2\pi(ul+vm)} dl dm, \quad (1)$$

where l, m represent the directional cosines of a vector (length d) in uvw coordinate with regard to the u and v axes. $A_f(l, m)$ signifies the effective collecting area of each antenna, and $I_f(l, m)$ denotes the intensity distribution at frequency f , which is the underlying subband's center frequency. This model is used in radio astronomy to estimate emissions from celestial bodies and sky brightness, i.e., $I_f(l, m)$ is measured by performing an inverse Fourier transform of (1). Because the emissions for space observations are considerably closer to the array, the visibilities must be refocused onto a certain distance and adapted for near-field transmission. Motivated by [16–18] we build and utilize the following model for visibilities refocused on distance d ,

$$v_{ij}(u, v, d) = \int_{-\infty}^{\infty} \int_{-\infty}^{\infty} A_f(l, m, d) I_f(l, m, d) c_i(l, m, d) c_j^H(l, m, d) dl dm, \quad (2)$$

Using the first-order near-field geometric model, we break down the visibility as the product of the phase components of the signal received at the i -th and j -th antennas,

$$c_i(l, m, d) = \exp(-j2\pi(-d_i^d + x_i^d l + y_i^d m - z_i)), \quad (3)$$

The main idea here is to assume different locations, i.e. (x, y, z) , for the antennas in uvw coordinates based on different hypotheses on the distance. For a given distance, d , we determine the locations, x_i^d, y_i^d , as

$$x_i^d = \frac{dx_i}{d_i^d}, \quad y_i^d = \frac{dy_i}{d_i^d}, \quad (4)$$

with d_i^d being

$$d_i^d = \sqrt{x_i^2 + y_i^2 + (z_i - d)^2}. \quad (5)$$

We discretize (2) by assuming that the observed intensity comes from K spatially-incoherent sources situated at (l_ℓ, m_ℓ, d_ℓ) such that $\ell \in [1, K]$,

$$v_{ij}(u, v, d) = \sum_{\ell=1}^K A_f(l_\ell, m_\ell, d_\ell) I_f(l_\ell, m_\ell, d_\ell) c_i(l_\ell, m_\ell, d_\ell) c_j^H(l_\ell, m_\ell, d_\ell),$$

and redefine it as a measurement vector

$$\mathbf{v}(u, v, d) = \mathbf{c}_i \mathbf{b} \mathbf{c}_j^H, \quad (6)$$

where

$$\begin{aligned} \mathbf{c}_i &= [c_i(l_1, m_1, d_1), \dots, c_i(l_K, m_K, d_K)] \quad 1 \times K, \\ \mathbf{b} &= \text{diag}\left(A_f(l_1, m_1, d_1) I_f(l_1, m_1, d_1), \dots, A_f(l_K, m_K, d_K) I_f(l_K, m_K, d_K)\right)^T \quad K \times K. \end{aligned}$$

It is possible to think of the correlation of the signals received by antennas i and j , indicated by (6), as an entry of a covariance matrix, i.e., $R_k[i, j] = v_{ij}(u, v, d)$. In reality, measurement noise and phase uncertainty affect the measurement vector in (6). For the sake of simplicity, we will assume that the phase uncertainty is small. Taking simply the noise into consideration, we have

$$\mathbf{R}[i, j] = \mathbf{c}_i \mathbf{b} \mathbf{c}_j^H + n_{i,j} \quad (7)$$

where $n_{i,j}$ is an additive term representing measurement noise in each antenna.

$$n_{i,j} = \begin{cases} 0 & i \neq j \\ \sigma^2 & i = j. \end{cases} \quad (8)$$

Lastly, we can put the whole measurement at epoch t into a matrix form by stacking the visibilities (correlation lags) on top of each other

$$\mathbf{R}(t) = \mathcal{A}(\mathbf{l}, \mathbf{m}, \mathbf{d}) \mathbf{b}(\mathbf{l}, \mathbf{m}, \mathbf{d}) \mathcal{A}^H(\mathbf{l}, \mathbf{m}, \mathbf{d}) + \sigma \mathbf{I}_N,$$

where

$$\begin{aligned} \mathcal{A}(t) &= [\mathbf{c}_1^T, \mathbf{c}_2^T, \dots, \mathbf{c}_N^T]^T, N \times K, \\ &= [\mathbf{a}_1; \mathbf{a}_2; \dots; \mathbf{a}_K], N \times K. \end{aligned} \quad (9)$$

To clarify, the phase vector of all K sources at the i -th lag is shown in the row vector \mathbf{c}_i , while the array steering vector towards the i -th intensity source is denoted by the vector \mathbf{a}_i .

$$\mathbf{a}_i = [c_1(l_i, m_i, d_i), \dots, c_N(l_i, m_i, d_i)]^T \quad N \times 1. \quad (10)$$

A linear measurement model in an array of antennas can be related to the covariance matrix in (9) as

$$\mathbf{y}(t) = \mathcal{A}(\mathbf{l}, \mathbf{m}, \mathbf{d}) \mathbf{b}(\mathbf{l}, \mathbf{m}, \mathbf{d}) + \mathbf{n}(t). \quad (11)$$

For the ℓ -th source, the unknown parameters to be identified are (l, m, d) and $b_\ell(l, m, d)$. In this study, the location parameters are the primary focus, and it is assumed that b_ℓ may be determined by these parameters. Subspace techniques can be used directly to the covariance matrix to get the parameters, keeping in mind that the interferometer provides the covariance matrix. We employ the MUSIC algorithm to create a 3D spectrum as

$$I_M(l, m, d) = \left(\mathbf{a}^T(l, m, d) (\mathbf{R}_n^s)^{-1} \mathbf{a}(l, m, d) \right)^{-1} \quad (12)$$

where the covariance matrix associated with the noise subspace is denoted by the symbol \mathbf{R}_n^s . The eigenvectors that span the noise subspace define the noise subspace. The K peaks of the 3D MUSIC spectrum show where the K sources are.

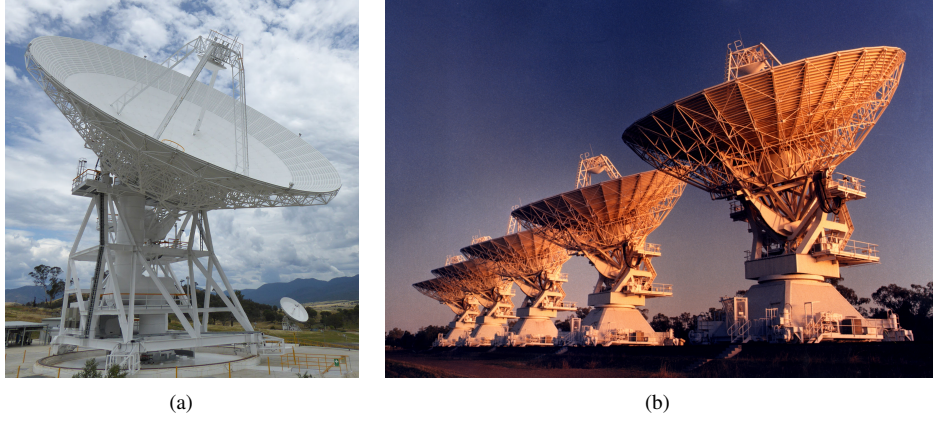


Fig. 1: (a) DSS 35 ©2022: Canberra Deep Space Communication Complex (CDSCC), (b) Five antennas of the Australia Telescope Compact Array (ATCA). Photo by John Masterson [19]

3. SYSTEM DESCRIPTION

To demonstrate interferometry-based localization using ATCA, we utilize a bi-static radar scenario with the Tx and Rx being roughly 566 km apart. The employed setup falls specifically under the bi-static radar interferometry category. On the transmit side, we use DSS-35, a 34-meter dish mainly used for deep space communications (see Fig.1(a)). For this experiment, DSS-35 was tasked to transmit a continuous wave (CW) signal at C-band.

On the receive side, we used ATCA comprising six 22-meter movable dishes (see Fig. 1(b)). The ATCA’s interferometer, aka Compact Array Broadband Backend (CABB) can correlate the received voltages at different antennas across a 4 GHz digital bandwidth and selected RF bands from 1.1 to 105 GHz. Given the total 4 GHz bandwidth, in interferometry mode, the correlation of each pair of antennas, i.e., *visibility* is computed for predefined subbands varying from 64 MHz down to 488 Hz. Regarding the integration cycle, the lowest resolution is 10 seconds, and the highest is 2 seconds in normal interferometry mode, where we have access to 488 Hz subbands. It is also possible to run ATCA in *tied-array* mode, where the *raw voltages* of a set of elements are combined and synced to a particular phase center from a single terrestrial coordinate. Since, as of now, there is no tested solution to record the voltages at multiple terrestrial locations, the set of tied elements provides merely a single array as big as the corresponding baseline, which makes it a good candidate for either Doppler processing as an individual sensor or interferometry with other telescopes in a very long baseline interferometry (VLBI) setup, but less useful as a standalone localization system.

As depicted in the block diagram in Fig. 2, we initiate the observation by a priori location information, i.e., the most recent TLE drawn from the North American Aerospace Defense Command (NORAD) database. Then, we supply the TLE to the Jet Propulsion Lab’s (JPL) Horizons System [20] and retrieve the geocentric RA and Dec of the RSO of interest and supply the ephemerides to ATCA’s pointing software to convert the geocentric coordinates to topocentric ones referenced to the correlator’s terrestrial coordinates. ATCA is then tasked to track the computed topocentric coordinate, i.e., phase center, through antenna pointing and delay tracking, and the visibilities are provided accordingly.

In post-processing, we do a phase center evaluation step to ensure that the delays have been tracked correctly. We compare the phase center of the observation as reported by ATCA against the a priori topocentric coordinates given by the Horizons System. The delay-tracking systematic error is then accounted for, and the visibilities are rotated appropriately so that the phase center matches that of the a priori. Having the corrected visibilities, the next step is to estimate new coordinates based on the range and directions estimated from the observation as explained in Section 2. Now we have the a priori coordinates as well as the refined ones, and we can compare them. In the absence of a *true* coordinate, we primarily discuss the *consistency* and *precision* of the entire system. Characterizing the *accuracy* would be available after running a measurement campaign involving a second sensor, e.g., optical and/or radar measurements.

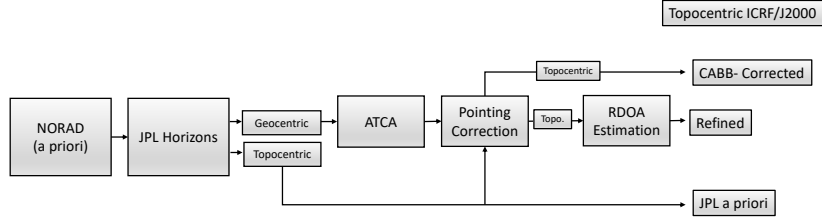


Fig. 2: System model and architecture of the evaluation method.

4. RDOA ESTIMATION METHOD

As introduced in Section 2, we apply a bespoke MUSIC algorithm to estimate a 3D spectrum for range and directions. In this section, we elaborate on the particular implementation we employ along with its parameters.

The RDOA estimation comprises three main steps 1) epoch filtering, 2) coarse estimation, and 3) fine estimation. As shown in Fig. 2, the visibilities are re-rotated first to remove any systematic pointing error and handed to the RDOA block. We would expect smoothly varying phases at this point, but there are several factors that can contaminate them, including self-generated or external interference, atmospheric effects, and the source being outside the main beam of the reflectors. Hence, we pick the *smooth* epochs, i.e., cycles, of phase measurements by analyzing the phase gradient. As shown in Fig. 3, we define a smooth region, e.g., $|\partial\theta/\partial t| < 5^\circ$ with θ being the phase, for the gradient of given visibility and select the measurements with values within the band. After selecting the smooth phases for each visibility, we define the epochs of interest as those with smooth phase measurements across all visibility pairs.

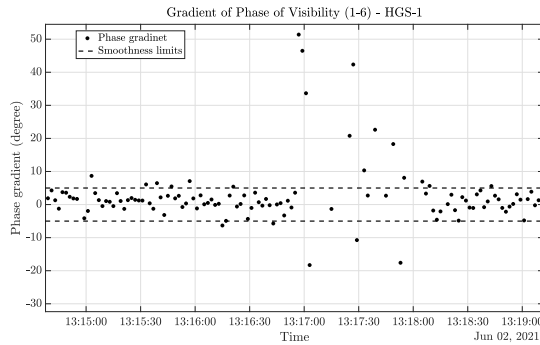


Fig. 3: Demonstration of phase smoothness analysis in visibility 1-6.

By filtering out the nonsmooth measurements, the smooth visibility pairs are employed to establish a covariance matrix for each epoch. To estimate the RDOA spectrum, we define a 3D grid comprising l , m , and d values. The estimation begins with a coarse step size of 2 arcseconds covering an angle of 200 arcseconds (100 steps) in both angular directions, and a dynamic resolution for the range. Although the reflector's field-of-view (FOV) provides a reasonable guide for the search area for the directions, determining such a measure for the range is not possible as there is no physical constraint on the range within which the signal is received from. Therefore, we define the minimum and maximum range of the search space based on the product of $(1 \pm 1/1000)$ and the mean range value around the epoch's a priori range. These range values are partitioned by 200 bins. For instance, for observing an RSO orbiting around 38000 km, the coarse range resolution is 380 meters within an area as wide as 76 km. The intensity is then calculated across the established 3D spectrum, and the peak provides a rough estimate for the coordinates.

We refine the estimate by zooming in and forming a higher resolution 3D spectrum around the coarse coordinates. The second stage grid comprises a 20 arcseconds by 20 arcseconds solid angle around the initial estimate with a resolution of 206 milliarcseconds. As for the range spectrum, we divide the gap between the initial and the a priori range values

Table 1: List of observed RSOs

RSO	NORAD ID
HGS-1	25126
GOES-9	23581
NAVSTAR-18	20452
ATLAS 5 CENTAUR R/B	40947

into ten bins. It is important to note that these parameters are not necessarily the optimal ones but are chosen such that we have the most consistent performance and a computationally manageable 3D search for the various experiments presented here.

5. RESULTS

We ran an experiment in June 2021. The array was in the H75 configuration as shown in Fig. 4, and the correlator was configured to provide 488 Hz zoom bands [21]. We designed a series of experiments to observe four targets in GEO and MEO as listed in Table. 1. The transmitter was tasked to track and illuminate the objects of interest using a circularly polarized CW signal in the C-band while ATCA tracked and received the echoes in both linear polarizations. A single linear polarization and single 488 Hz subband have been utilized for the results presented below. The data has also gone through the normal astronomy online calibration and offline bandpass calibration.

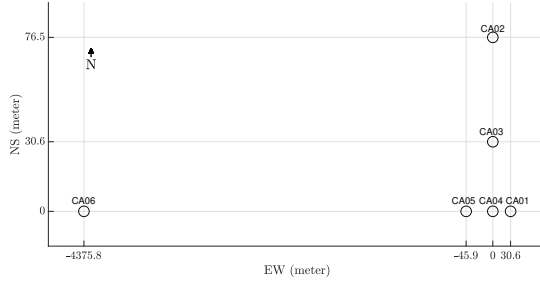


Fig. 4: Array configuration during the experiment.

5.1 HGS-1

HGS-1 was retired in 2002 and parked in the graveyard orbit. HGS-1's total mass is estimated at around 1700 kg, and its total span is estimated at roughly 14.4 meters, assuming one of the solar panels is stowed [22]. We show the estimated directions and range offsets from the NORAD TLE in the international celestial reference frame (ICRF) in Figs. 5, and 6. For direction offsets, we show both the initial datapoints and the fitted curve for better presentation. As can be seen in Fig. 5 the direction estimates are spread across about 5 arcseconds around the fitted curve, potentially due to atmospheric effects and ambiguities with multiple peak detections. For range, we fit a curve to the qualifying estimates sitting at the central 50 percent of the distribution, demonstrating the estimates exhibit no bias with respect to the a priori range values.

The phase of two pairs of visibilities for the longest (1-6) and the shortest (1-4) baselines are depicted in Figs. 7 and 8 respectively. The impact of the coordinate refinement achieved by the proposed method is demonstrated in Fig. 7 where we show how the phases are stabilized in two stages. Starting from the measured phases, which wrap due to a systematic pointing error (black dots), we re-rotate them to the expected coordinate to get more stable phases (blue circles). Our system is now correctly tracking the a priori location estimate. However, the phases are not yet stable due to the direction and range offsets, providing consistent delay tracking. After re-rotating the visibility to the refined coordinates shown in Fig. 5, and 6, we will have a significantly more stable phase behavior as depicted by green filled circles in Fig. 7(a). The statistical distribution of the phases is shown in Fig. 7(b). As can be seen in the top panel of Fig. 7(b) the phases are spread across the bins, representing the full circle (i.e. 360°) wrapping in Fig. 7(b). However,

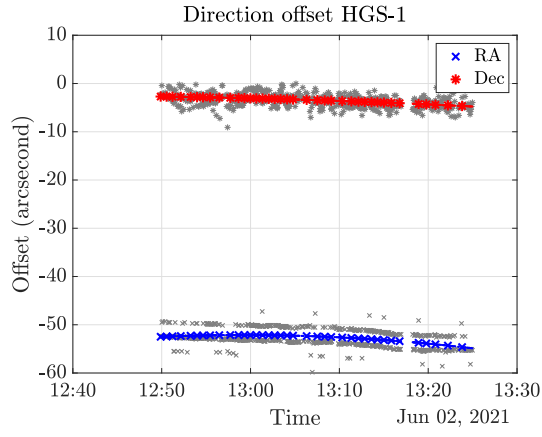


Fig. 5: RA and Dec offsets for HGS-1.

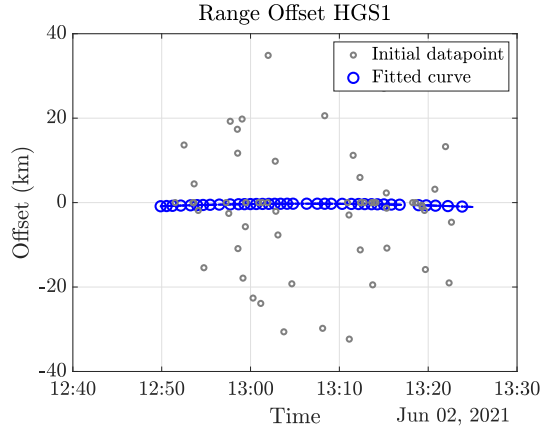


Fig. 6: Range offset for HGS-1.

as depicted in the bottom panel of Fig. 7(b) the phases are distributed with 3.56 degrees of standard deviation after refining the location, demonstrating the precision of the measurement.

The impact of coordinate refinement on phase stabilization is less pronounced for the 1-4 baseline, as shown in Fig. 8 due to the effective aperture being significantly smaller (30.6 meters vs. 4375.8 meters for 1-6 baseline). While the phase becomes almost stable after re-rotating towards the expected coordinate, the location refinement improves the stability only marginally by reducing the standard deviation from 2.68 to 2.62 degrees.

5.2 GOES-9

GOES-9 is a satellite from the Geostationary Operational Environmental Satellite (GOES) constellation decommissioned in 2007 and boosted into the graveyard orbit. Taking the magnetometer boom into account, it spans 10.6 meters [23]. We show the direction offsets in Fig. 9 as well as range offset in Fig. 10. Similar to HGS-1, we see fluctuations in both directions and range estimates with more valid range data points available.

As shown in Fig. 11(a), applying the location estimate to the re-rotation method stabilizes the phase of baseline 1-6. However, the phase still varies around 180 degrees in almost 30 minutes. The phase instability can be associated with inherent limitations caused by the available 2-second integration cycle of ATCA's correlator such that when the RA and Dec vary relatively fast within 2 seconds, rotating towards the middle point does not make the phase stable enough as the phase center is varying significantly across the cycle. Although this slope exists in Fig. 7(a) as well, it is not significant due to the smaller RA and Dec rates (15.3 arcseconds RA and -1.7 arcseconds Dec per second for HGS-1 versus 18.37 arcseconds RA and -4 arcseconds Dec per second for GOES-9). As we see in Fig. 8(a) the phase of visibility associated with baseline 1-4 gets slightly more stabilized after location refinement and the standard deviation reduces from 3.5 to 3.1 degrees.

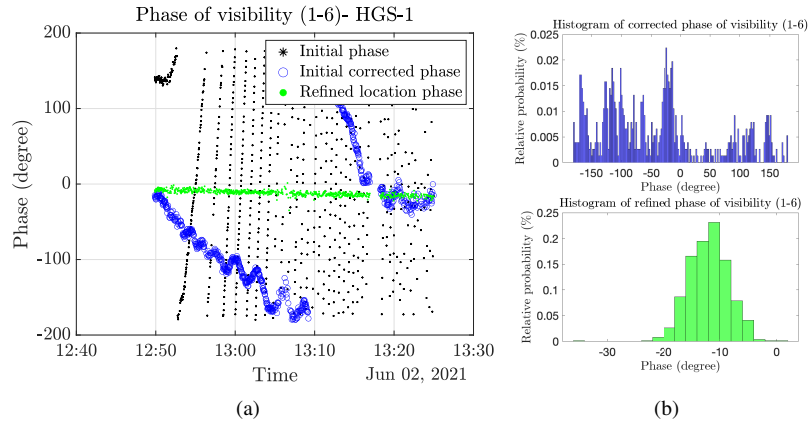


Fig. 7: (a) Phase of visibility associated with antenna 1 and 6 in different stages , (b) (Top) Histogram of the phase values after re-rotation towards the expected coordinates, (Bottom) Histogram of the phase values after re-rotation towards the refined coordinates.

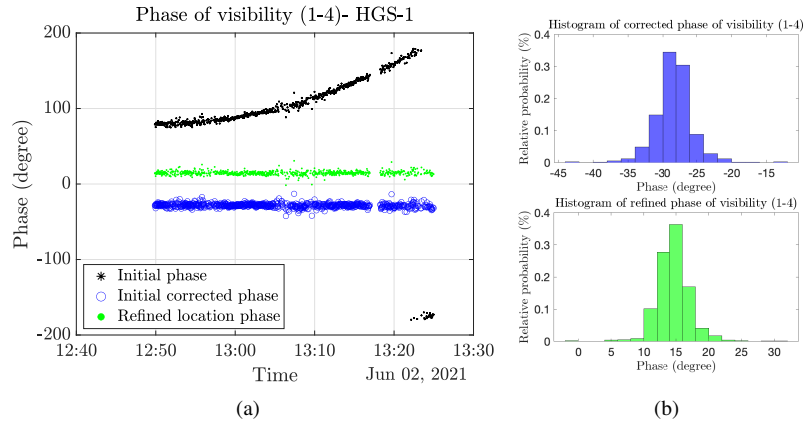


Fig. 8: (a) Phase of visibility associated with antenna 1 and 4 in different stages for HGS-1, (b) (Top) Histogram of the phase values after re-rotation towards the expected coordinates, (Bottom) Histogram of the phase values after re-rotation towards the refined coordinates.

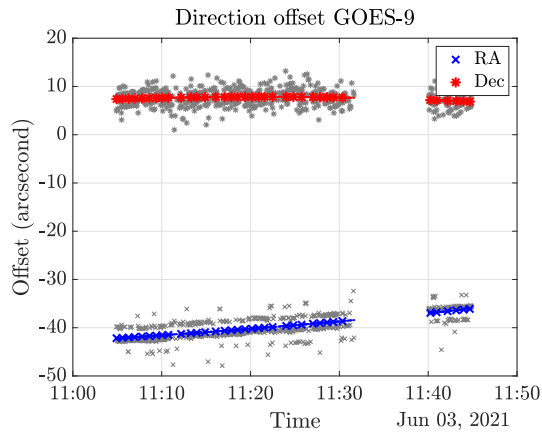


Fig. 9: RA and Dec offsets for GOES-9.

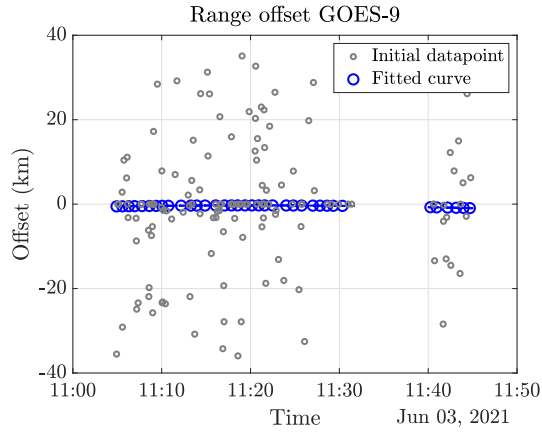


Fig. 10: RA and Dec offsets for GOES-9.

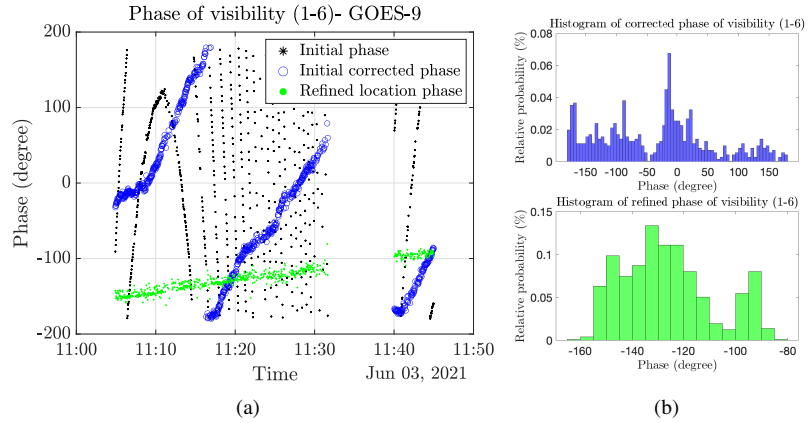


Fig. 11: (a) Phase of visibility associated with antenna 1 and 6 in different stages for GOES-9 , (b) (Top) Histogram of the phase values after re-rotation towards the expected coordinates, (Bottom) Histogram of the phase values after re-rotation towards the refined coordinates.

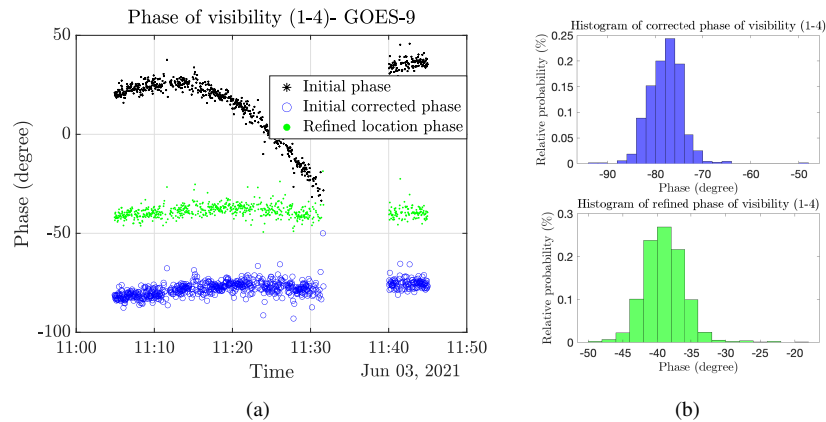


Fig. 12: (a) Phase of visibility associated with antenna 1 and 4 in different stages for GOES-9 , (b) (Top) Histogram of the phase values after re-rotation towards the expected coordinates, (Bottom) Histogram of the phase values after re-rotation towards the refined coordinates.

5.3 NAVSTAR-18

NAVSTAR-18 was part of the Global Positioning System (GPS) block II which was launched in 1991 and retired in 2000. The satellite had a total launch mass of 850 kg and spans 5.3 meters across with deployed solar panels, and currently is in MEO [24]. The direction and range offsets are shown in Figs 13, and 14. The precision of the direction estimates is more visible in Fig 13 which is in line with the spread of the antenna locations across u and v axes. Given that the locations spread across the diagonal of a hypothetical rectangle with u , i.e., RA, across the length, a beamformed array pattern would have an elliptical shape along the diagonal. Therefore, there is potentially a higher resolution for RA estimates as well as more ambiguities, as shown in Fig. 13.

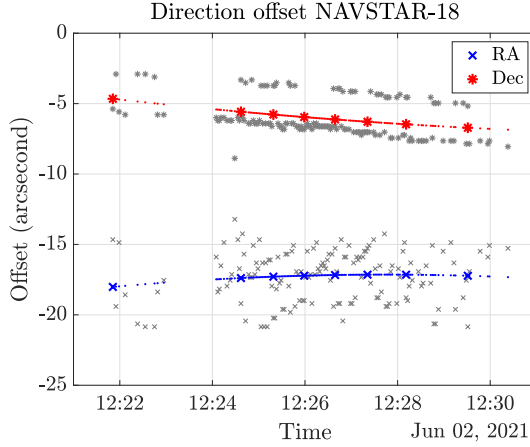


Fig. 13: RA and Dec offsets for NAVSTAR-18.

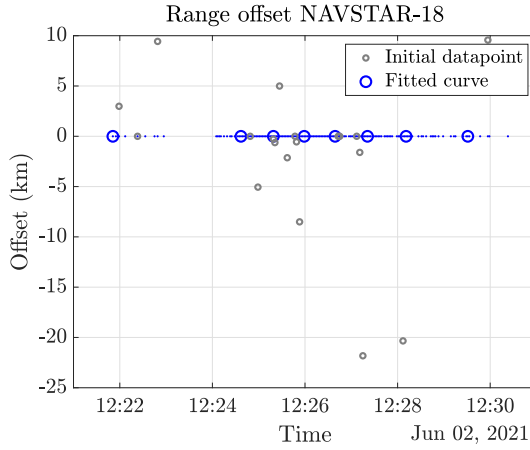


Fig. 14: Range offset for NAVSTAR-18.

The phase of visibility 1-6 becomes relatively more stable after applying the refined coordinates, as shown in Fig. 15(a), and the standard deviation reduces from 46 to 10 degrees. As shown in Fig. 16(a) the impact of location refinement is minor over the 1-4 baseline, which is in line with the smaller magnitude of the direction offsets compared to HGS-1 and GOES-9 observations.

5.4 ATLAS 5 CENTAUR R/B

ATLAS 5 CENTAUR R/B (2015-056B) is known to be a discarded Atlas V Centaur booster, i.e., rocket body. Atlas V comprises the main booster with a length of 32.46 meters and a diameter of 3.81 meters, and the solid rocket boosters (SRBs) measuring 20 meters in length and 1.58 meters in diameter [25], and the authors are unsure which part of the rocket this object is. During 40 minutes of the experiment, 2015-056B descended about 6000 kilometers in range (see Fig. 18(b)) due to its elliptical orbit. The direction and range offsets are shown in Figs. 17, and 18(a) with more outliers due to the fast location variations.

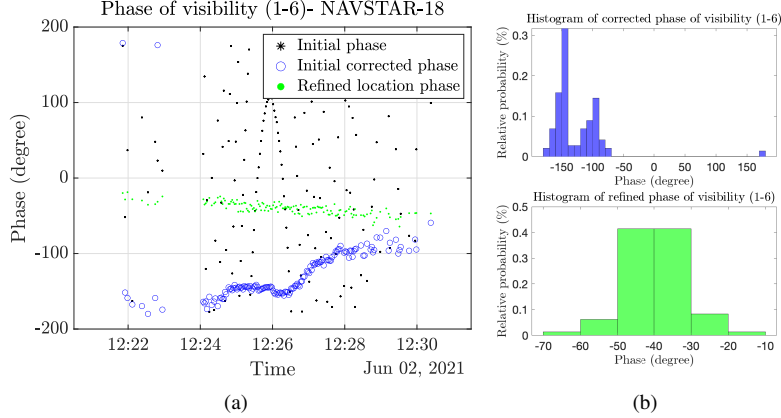


Fig. 15: (a) Phase of visibility associated with antenna 1 and 6 in different stages for NAVSTAR-18 , (b) (Top) Histogram of the phase values after re-rotation towards the expected coordinates, (Bottom) Histogram of the phase values after re-rotation towards the refined coordinates.

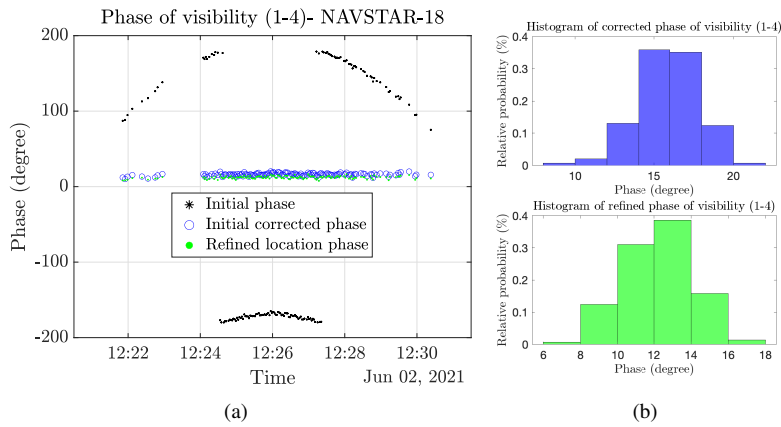


Fig. 16: (a) Phase of visibility associated with antenna 1 and 4 in different stages for NAVSTAR-18 , (b) (Top) Histogram of the phase values after re-rotation towards the expected coordinates, (Bottom) Histogram of the phase values after re-rotation towards the refined coordinates.

The phase of the visibility associated with antennas 1-6 is shown in Fig. 19(b) demonstrating the effectiveness of both initial correction and location refinement by reducing the standard deviation from 97 to 56 degrees. Furthermore, a slight improvement is achieved in baseline 1-4 as shown in Fig. 20(b) in by reducing the standard deviation from 10 to 9 degrees. It is worth noting that the impact of the integration cycle is clearer here, such that with 62.65 and -9.05 arcseconds per second for RA and Dec, not only is the phase instability clearly present in the shortest baseline, it can not be much improved after applying the refined coordinates.

6. CONCLUSION

We employed the Australia Telescope Compact Array (ATCA), and a Deep Space Network (DSN) station to refine the coordinates of resident space objects (RSOs) at geostationary orbit (GEO) and medium earth orbit (MEO). We developed a bespoke method to estimate the range and direction of arrival (DOA) of orbital radio sources based on the interferometric data provided by a correlator radio telescope and studied the performance by analyzing the data from measurement campaigns in June 2021. We demonstrated that the new coordinates could be determined in terms of the range and direction offsets within the estimated 3D spectrum. Also, through analyzing the stability of the phase of the visibilities, i.e., correlation lags, we demonstrated that the measurement precision improves significantly after applying the refined coordinates.

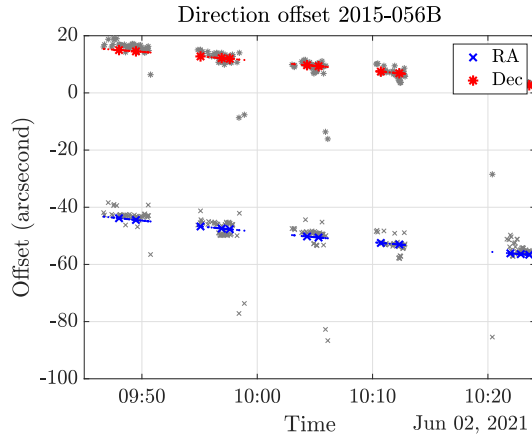


Fig. 17: RA and Dec offsets for ATLAS 5 CENTAUR R/B.

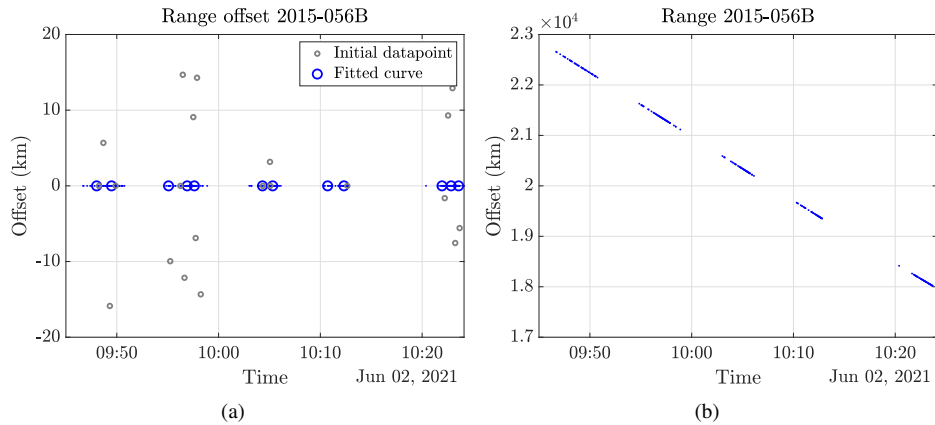


Fig. 18: (a) Range offset for ATLAS 5 CENTAUR R/B , (b) a priori range for ATLAS 5 CENTAUR R/B.

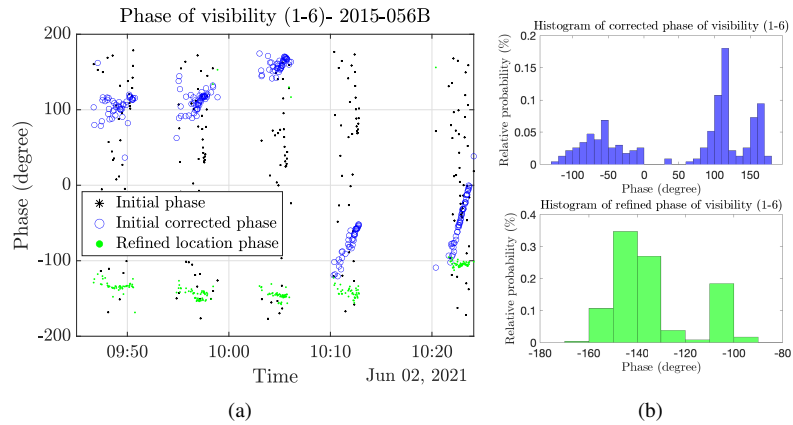


Fig. 19: (a) Phase of visibility associated with antenna 1 and 4 in different stages for ATLAS 5 CENTAUR R/B , (b) (Top) Histogram of the phase values after re-rotation towards the expected coordinates, (Bottom) Histogram of the phase values after re-rotation towards the refined coordinates.

REFERENCES

- [1] T. Maclay and D. McKnight, “Space environment management: Framing the objective and setting priorities for controlling orbital debris risk,” *Journal of Space Safety Engineering*, vol. 8, no. 1, pp. 93–97, mar 2021.

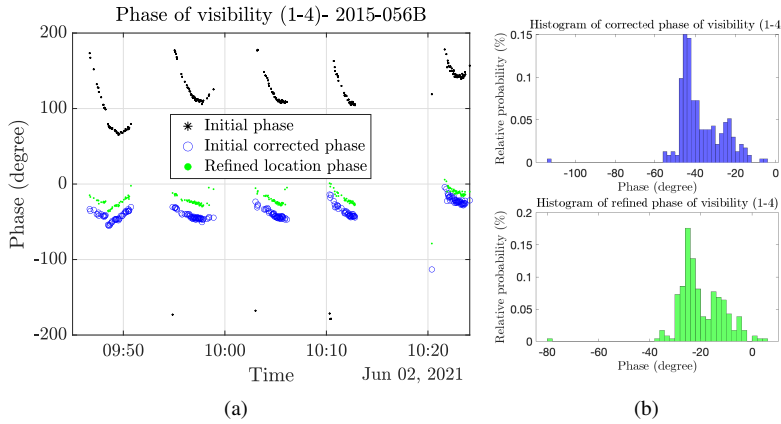


Fig. 20: (a) Phase of visibility associated with antenna 1 and 4 in different stages for ATLAS 5 CENTAUR R/B , (b) (Top) Histogram of the phase values after re-rotation towards the expected coordinates, (Bottom) Histogram of the phase values after re-rotation towards the refined ephemerides.

- [2] T. J. Muelhaupt, M. E. Sorge, J. Morin, and R. S. Wilson, “Space traffic management in the new space era,” *Journal of Space Safety Engineering*, vol. 6, no. 2, pp. 80–87, jun 2019.
- [3] D. A. Vallado, *Fundamentals of Astrodynamics and Applications*, 4th ed. Microcosm Press, Hawthorne, CA, 2013.
- [4] D. A. Vallado and J. D. Griesbach, “Simulating space surveillance networks,” in *Paper AAS 11-580 presented at the AAS/AIAA Astrodynamics Specialist Conference*. July, 2011.
- [5] H. Wilden, C. Kirchner, O. Peters, N. B. Bekhti, A. Brenner, and T. Eversberg, “GESTRA — a phased-array based surveillance and tracking radar for space situational awareness,” in *2016 IEEE International Symposium on Phased Array Systems and Technology (PAST)*. IEEE, oct 2016.
- [6] M. Nicolls, V. Vittaldev, D. Ceperley, J. Creus-Costa, C. Foster, N. Griffith, E. Lu, J. Mason, I. Park, C. Rosner *et al.*, “Conjunction assessment for commercial satellite constellations using commercial radar data sources,” in *Advanced Maui Optical and Space Surveillance (AMOS) Technologies Conference*, 2017, p. 18.
- [7] J. Yu, S. Cho, and J. H. Jo, “KOSPAW test bed—a phased array radar for space situational awareness,” in *2020 IEEE International Radar Conference (RADAR)*. IEEE, apr 2020.
- [8] P. W. Schumacher, “US naval space surveillance upgrade program 1999–2003,” in *7th US/Russian Space Surveillance Workshop Proceedings, Naval Postgraduate School, CA*, vol. 29, 2007.
- [9] D. Mehrholz, L. Leushacke, and R. Jehn, “The COBEAM-1/96 experiment,” *Advances in Space Research*, vol. 23, no. 1, pp. 23–32, 1999. [Online]. Available: <https://www.sciencedirect.com/science/article/pii/S0273117798002269>
- [10] G. Muntoni, L. Schirru, T. Pisanu, G. Montisci, G. Valente, F. Gaudiomonte, G. Serra, E. Urru, P. Ortu, and A. Fanti, “Space debris detection in low earth orbit with the Sardinia Radio Telescope,” *Electronics*, vol. 6, no. 3, p. 59, aug 2017.
- [11] Losacco and Schirru, “Orbit determination of resident space objects using the P-Band mono-beam receiver of the Sardinia Radio Telescope,” *Applied Sciences*, vol. 9, no. 19, p. 4092, sep 2019.
- [12] J. E. Palmer, B. Hennessy, M. Rutten, D. Merrett, S. Tingay, D. Kaplan, S. Tremblay, S. Ord, J. Morgan, and R. B. Wayth, “Surveillance of space using passive radar and the Murchison Widefield Array,” in *2017 IEEE Radar Conference (RadarConf)*. IEEE, may 2017.
- [13] B. Hennessy, S. Tingay, P. Hancock, R. Young, S. Tremblay, R. B. Wayth, J. Morgan, S. McSweeney, B. Crosse, M. Johnston-Hollitt, D. L. Kaplan, D. Pallot, and M. Walker, “Improved techniques for the surveillance of the near earth space environment with the Murchison Widefield Array,” in *2019 IEEE Radar Conference (RadarConf)*. IEEE, apr 2019.
- [14] P. Stoica and A. Nehorai, “MUSIC, maximum likelihood, and Cramer-Rao bound,” *IEEE Transactions on Acoustics, Speech, and Signal Processing*, vol. 37, no. 5, pp. 720–741, 1989.
- [15] A. R. Thompson, J. M. Moran, and G. W. Swenson, *Interferometry and synthesis in radio astronomy*. Springer Nature, 2017.

- [16] T. Cornwell, “The correction of near field effects in radio interferometric geolocation,” 2004. [Online]. Available: <https://citeseerx.ist.psu.edu/viewdoc/summary?doi=10.1.1.114.5643>
- [17] J. Lazio, “On near-field w-projection for radio interferometric imaging,” NAVAL RESEARCH LAB WASHINGTON DC REMOTE SENSING DIV, Tech. Rep., 2009.
- [18] W. Carter, “On refocusing a radio telescope to image sources in the near field of the antenna array,” *IEEE Transactions on Antennas and Propagation*, vol. 37, no. 3, pp. 314–319, 1989.
- [19] CSIRO, “Five antennas at Narrabri,” 2013, [Accessed 2022-08-23]. [Online]. Available: <https://www.scienceimage.csiro.au/image/3881>
- [20] J. Giorgini and JPL Solar System Dynamics Group, “Nasa/jpl horizons on-line ephemeris system.” [Online]. Available: <https://ssd.jpl.nasa.gov/horizons/>
- [21] J. Stevens, R. Wark, P. Edwards, S. Breen, K. Lee-Waddell, J. Kaczmarek, and G. Heald, “ATCA Users Guide,” 2022. [Online]. Available: https://www.narrabri.atnf.csiro.au/observing/users_guide/html/atug.html
- [22] M. A. Earl and G. A. Wade, “Observations of the spin-period variations of inactive box-wing geosynchronous satellites,” *Journal of Spacecraft and Rockets*, vol. 52, no. 3, pp. 968–977, may 2015.
- [23] C. R.L., “Rotation rates of inactive satellites near geosynchronous earth orbit,” in *Proceedings of the Advanced Maui Optical and Space Surveillance Technologies Conference*, Wailea, Hawaii, 2014.
- [24] “Navstar 2-06 in NASA Space Science Coordinated Archive.” [Online]. Available: <https://nssdc.gsfc.nasa.gov/nmc/spacecraft/display.action?id=1990-008A>
- [25] *Atlas V Launch Services User’s Guide*, ULA, Mar. 2010.